Construction and performance test of the drift chambers at the target area of the External Target Facility of CSR*

X. Jiang,[1,2] Y.Z. Sun,[1] S.T. Wang,[1,2,†] Z.Y. Sun,[1,2,‡] P. Ma,[1,2] L.M. Duan,[1,2] F.H. Lu,[1] S.Y. Jin,[1] S.W. Tang,[1,2] Y.H. Yu,[1,2] X.H. Zhang,[1,2] X.D. Xu,[1,2] H.J. Ong,[1,2] D. Yan,[1,2] F. Fang,[1,2] Y.J. Zhang,[1,2] X.L. Tu,[1,2] X.B. Wei,[1,3] Z.Y. Li,[1,2] T.Q. Liu,[1] Y.F. Xu,[1] L.F. Wan,[1,2] G.L. Zhang,[1,2] J.L. Zhang,[1,4] J.B. Long,[1,2] and Z.X. Wang[1,3]

[1] *Institute of Modern Physics, Chinese Academy of Sciences, Lanzhou 730000, China*
[2] *School of Nuclear Science and Technology, University of Chinese Academy of Sciences, Beijing 100049, China*
[3] *College of Physics, Henan Normal University, Xinxiang 453007, China*
[4] *College of Physics and Electronic Engineering, Northwest Normal University, Lanzhou 730070, China*

The multiwire drift chambers at the target area of the External Target Facility of CSR are constructed for tracking radioactive ion beams that enter and exit the target. Two drift chambers with a sensitive area of $8\times8\,\mathrm{cm}^2$ are positioned upstream of the target, while another two drift chambers with a sensitive area of $16\times16\,\mathrm{cm}^2$ are placed upstream of the target. The drift chambers were tested using 350 MeV/u ^{78}Kr beams and cocktail secondary beams. To improve drift time precision, the time walk effect is corrected by using the measured energy. The impact of δ-rays on the multiplicity and spatial resolution is assessed using beams with various atomic number and different applied voltages. The optimal voltage to minimize the impact of δ-rays is obtained. An optimal spatial resolution of 35 μm for the drift chambers is achieved.

Keywords: drift chamber, track reconstruction, spatial resolution, radioactive ion beam, δ-ray

I. INTRODUCTION

Multiwire drift chambers are widely used in nuclear physics experiments to track charged particles. They have high detection efficiencies and can measure the position of ions with good spatial resolution, typically around a few hundred μm or even better [1–3]. Drift chambers have been broadly employed in large-acceptance spectrometers for radioactive ion beam physics experiments, such as SUMARAI [4] at the RIKEN RI Beam Factory (RIBF), S800 [5] at the National Superconducting Cyclotron Laboratory (NSCL), and the External Target Facility (ETF) [6–8] at the Heavy Ion Research Facility in Lanzhou-Cooler Storage Ring (HIRFL-CSR) [9–11].

The ETF is designed for studies on nuclear structure and reactions involving radioactive ion beams (RIBs) that are produced by the second Radioactive Ion Beam Line in Lanzhou (RIBLL2) [12–14]. A schematic illustration of the setups at the ETF target area is shown in Fig.1. At the ETF target area, two sets of target-front drift chambers (FDCs) and two sets of target-rear drift chambers (RDCs) are developed. Their purpose is to reconstruct the tracks of particles before and after they bombard the reaction target. Two multiple sampling ionization chambers, named MUSIC1 and MUSIC2 [15, 16], are positioned respectively before and after the target to measure the energy loss (ΔE) of incident and outgoing particles. A plastic scintillator is installed in front of FDC1 to measure beam arrival time. Particle identification at the ETF is achieved through the $B\rho$–TOF–ΔE method [17]. The $B\rho$ value is obtained from track reconstruction, which is based on the positions and angles of particles measured by the tracking detectors before and after the large gap magnet (not shown in Fig.1). Therefore, the spatial resolution of drift chambers is crucial for precising particle identification [18, 19].

This paper offers a comprehensive description of the construction of the target area drift chambers and highlights the results from beam tests. Section 2 delves into the design details of both the FDCs and RDCs. Section 3 describes the conditions of the beam tests. In Section 4, we focus on the determination of drift time, with a particular emphasis on the method developed to correct for the time walk effect. Section 5 explores the influence of δ-rays under varying applied voltages and beam conditions, as well as their relationship to atomic number. The discussion in Section 6 centers on the multiplicity of drift chambers, examining how different voltages and atomic numbers affect its performance. Section 7 outlines the method used to derive the space-time (r-t) relation. Finally, Section 8 presents the track fitting method, investigates the spatial resolution under various conditions, and provides the optimal spatial resolution achievable in the drift chamber at the optimal voltage.

II. DESIGN OF THE DRIFT CHAMBERS

The two FDCs are identical and have a sensitive area of $8\times8\,\mathrm{cm}^2$. Similarly, the two RDCs are also identical and have a sensitive area of $16\times16\,\mathrm{cm}^2$. The downstream RDCs are designed larger in size than the upstream FDCs, since the reaction products may exit at a large angle. Although both types of drift chambers differ in size, they share the same structure.

Each FDC (RDC) consists of two sub-drift chambers, which are responsible for measuring positions in the x and y directions, respectively (see Fig.2). The wires in the two sub-drift chambers are arranged perpendicular to each other. Except for the wire orientations, all other parameters of the

* This work was supported by the National Key R&D Program of China (Grant No. 2023YFA1606400), the National Natural Science Foundation of China (Nos. 12475125, and 12375186), and Longyuan Young Talents Project.
† Corresponding author, wangshitao@impcas.ac.cn
‡ Corresponding author, sunzhy@impcas.ac.cn

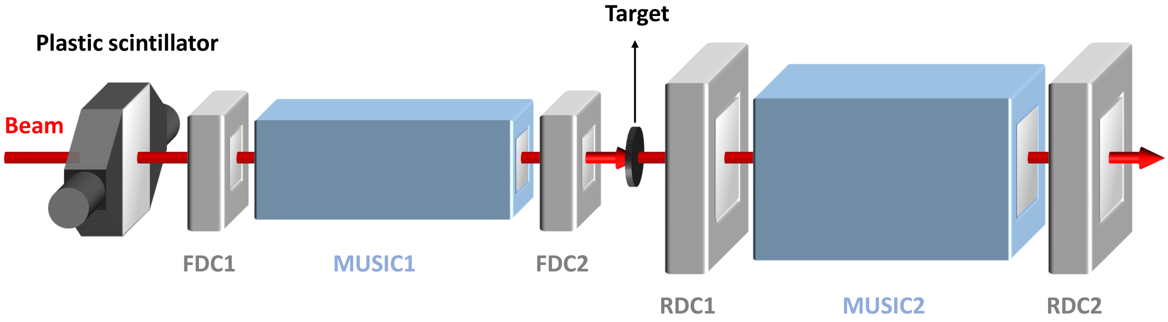

Fig. 1. The schematic diagram of the setups at the ETF target area.

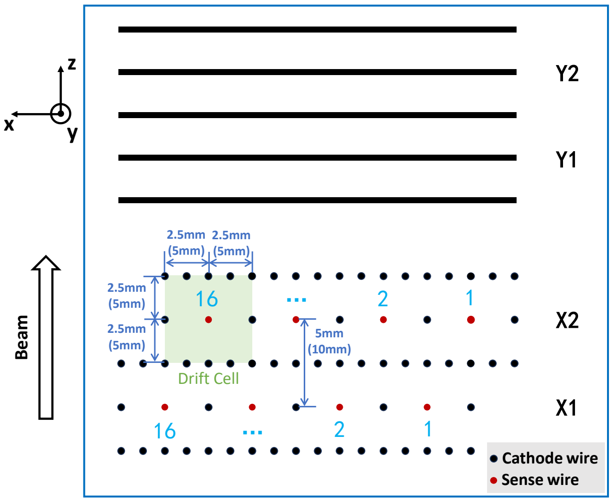

Fig. 2. Top-view diagram of the wire layout inside FDC and RDC. The parameters of the FDC (RDC) are shown without (within) parentheses.

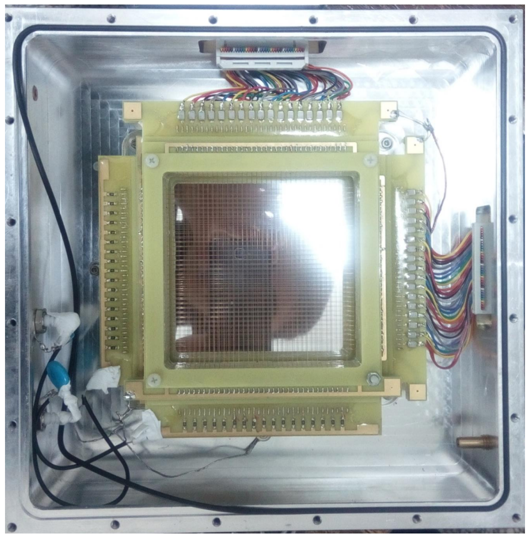

Fig. 3. Photo of the internal structure of the FDC.

two sub-drift chambers are identical. Each sub-drift chamber contains five layers of wires, with two layers of sense wires and three layers of cathode wires arranged alternately. The four sense wire layers are aligned along the beam direction in the order of X1, X2, Y1 and Y2. The spacing between the X1 and X2 layers in the FDCs (RDCs) is 5 mm (10 mm), and the same is true of the Y1 and Y2 layers. Furthermore, the distance between each sense wire layer and its adjacent cathode wire layers is 2.5 mm (5 mm). The sense wires in the FDCs (RDCs) are 20 μm gold-plated tungsten wires, while the cathode wires are 75 μm (100 μm) copper-tungsten alloy wires.

In FDCs (RDCs), the sense wires and field wires (using the same wires as the cathode wires) are alternately arranged with a spacing of 2.5 mm (5 mm) between the wires (see Fig.2) to ensure a uniform electric field within each cell. Accordingly, the area of each drift cell is $5 \times 5\,\mathrm{cm}^2$ ($10 \times 10\,\mathrm{cm}^2$) for FDCs (RDCs). Furthermore, the X1 layer and X2 layer are offset by 2.5 mm (5 mm) to address the leftright ambiguity in the drift chambers, with the same offset applied to Y1 layer and Y2 layer.

The working gas used in the drift chambers is a mixture of 80% argon and 20% carbon dioxide at room temperature and atmospheric pressure with the gas flow mode. The drift chamber windows, made of 25 μm thick aluminum-plated Kapton film, serves the function of separating the ambient air from the working gas. During operation, a positive voltage is applied to the sense wires, while the cathode wires are kept grounded. The specifications of the FDCs (RDCs) are provided in Table 1, and Fig.3 shows an internal photograph of the actual drift chamber.

Each layer of sense wires in the FDCs (RDCs) outputs signals to 16 readout channels, totaling 64 channels per chamber. The readout signals from the sense wires are am-

Table 1. Parameters of the FDC (RDC).

Sense wire configuration	X1X2-Y1Y2
Effective area [mm^2]	80×80 (160×160)
Cell size [mm^2]	5×5 (10×10)
Sense wire	Au-plated W, 20 μm in diameter
Cathode wire	Cu-Be, 75 (100) μm in diameter
Counter gas	80% Ar + 20% CO_2
Gas shield window	25 μm thick Al-Kapton $\times$ 2

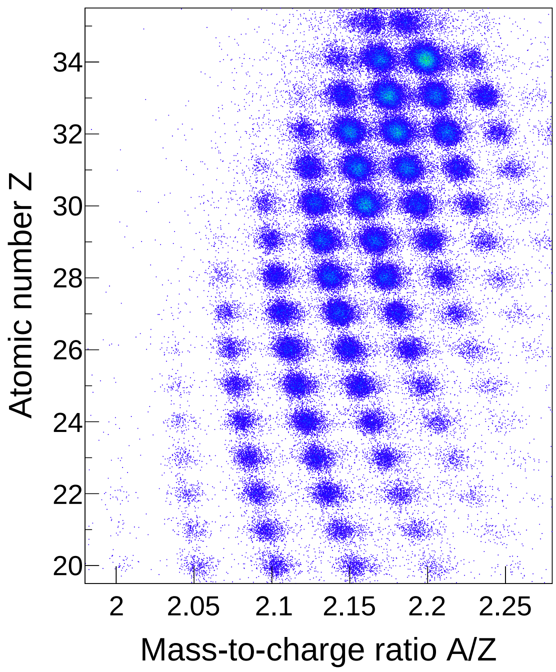

Fig. 4. The particle identification spectrum of the secondary beams used to test the drift chambers.

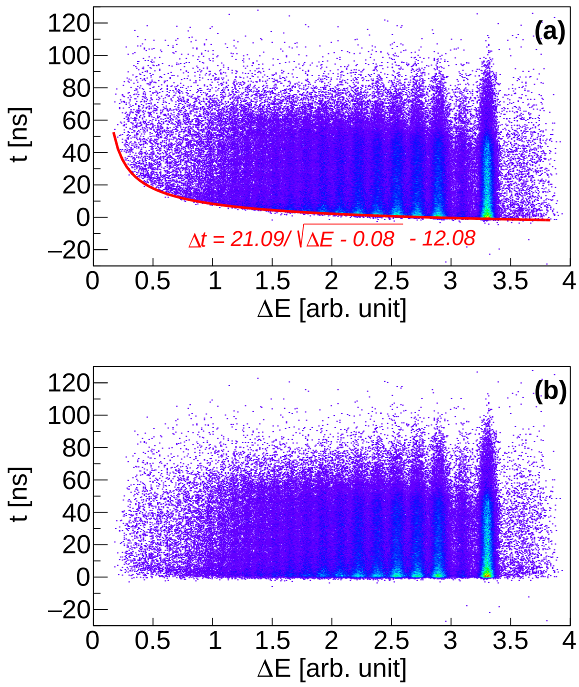

Fig. 5. Drift time-ΔE relation of FDC (a) before time walk correction and (b) after time walk correction.

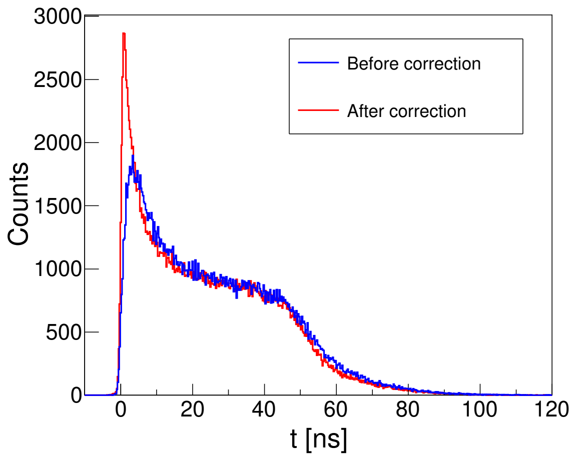

Fig. 6. Drift time distribution spectra of FDC before and after time walk correction.

plified and discriminated by the charge-sensitive amplifier shaper discriminator SFE16 [20] chips. The time digitization is achieved using the high-performance time-to-digital converter (HPTDC) [21], which records the leading and trailing times of the signals in high-resolution mode, offering a resolution of 100 ps [22].

III. EXPERIMENTAL TEST CONDITIONS

The performance of the drift chambers are detailed evaluated in a test experiment using 350 MeV/u ^{78}Kr primary beams and a series for secondary beams with the atomic number Z from 20 to 36 produced by the fragmentation of ^{78}Kr ions. The particle identification spectrum of the secondary beams delivered by RIBLL2 and used in this test is presented in Fig.4.

In order to ascertain the impact of voltage on the performance of the drift chamber, a series of voltage levels were applied during the test. The voltage settings used for the primary beam tests were $U = 650$ V, 700 V, 750 V and 800 V. In the secondary beam test, the voltage settings were $U = 650$ V, 750 V, 850 V, and 900 V.

IV. DRIFT TIME AND CORRECTION FOR TIME WALK

The drift time in the drift chambers is obtained by subtracting the time measured by the plastic scintillator from the time recorded by the drift chambers. Because beams with different atomic numbers deposit different amounts of energy loss ΔE in the drift chambers and the time measured by the drift chambers is determined using leading edge discrimination method, a significant time walk effect occurs for beams with large charge differences. Particles with larger ΔE in the drift chambers exhibit steeper signal leading edges, resulting in shorter measured drift time. To ensure that particles with different ΔE can use the same r-t relation under identical conditions, the time walk correction is necessary.

The energy loss of the particles in the FDCs (RDCs) is cor-

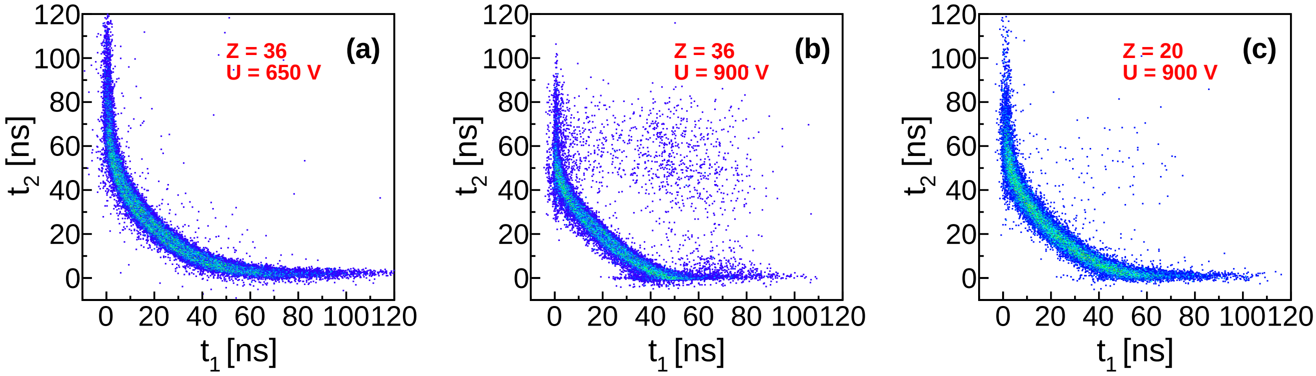

Fig. 7. Scatter plot of FDC's drift time of two wire layer X1 (t_1) and X2 (t_2) with (a) $Z = 36$ and $U = 650$ V; (b) $Z = 36$ and $U = 900$ V; (c) $Z = 20$ and $U = 900$ V.

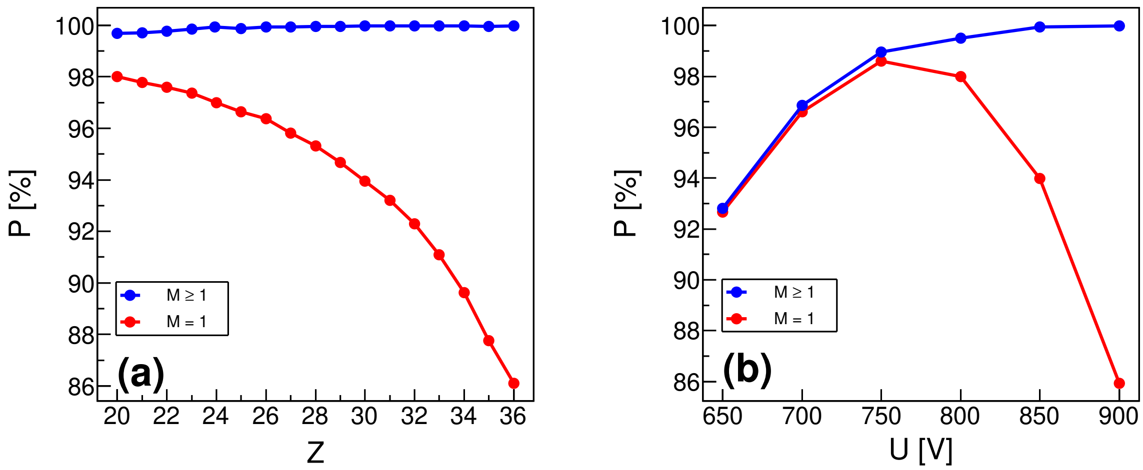

Fig. 8. Proportion of $M \geq 1$ and $M = 1$ as functions of (a) Z at $U = 900$ V and (b) U at $Z = 36$ for FDC.

related with the energy loss ΔE measured by MUSIC1 (MUSIC2) placed upstream (downstream) of the target (see Fig.1). As an example, the relation of drift time and ΔE for the FDC in the secondary beam test at a voltage of 900 V is shown in Fig.5(a). The starting points in the drift time spectra for different isotopes should be the same and be at 0 ns. However, because of the time-walk effect, the drift time starting points for the particles exhibit a curved relationship with ΔE, as shown in Fig.5(a).

The relationship between ΔE and the starting points of drift time is fitted using a square root function: $\Delta t = a/\sqrt{\Delta E + b} + c$. And the corrected drift time can be obtained by $t = t_0 - \Delta t$, where t_0 is the original drift time.

After the correction for the time walk, the drift time starting points are independent of energy loss, as can be seen in Fig.5(b). Moreover, the leading edge of the drift time spectrum becomes steeper after correction, as demonstrated in Fig.6.

V. IMPACT OF δ-RAYS

When heavy ions pass through the drift chamber, high-energy δ-rays may be generated [23, 24]. If the voltage is too high, δ-ray signals may be acquired simultaneously with the beam signals and negatively affect the drift time. We use different beams and apply various voltages to systematically investigate the impact of δ-rays on the drift time. The best voltage conditions to reduce the δ-ray effect for each kind of beams are evaluated.

Fig.7 shows the relation between the drift time (t_1) measured by X1 layer and that (t_2) by X2 layer in the FDC under different conditions: (a) $U = 650$ V and $Z = 36$; (b) $U = 900$ V and $Z = 36$; (c) $U = 900$ V and $Z = 20$. Since the beam is generally incident vertically to the detector, if the particle's incident position is close to one layer of wires, it will consequently be farther from another layer of wires. As a result, the t_1-t_2 distribution for adjacent two wires in different layers ideally should form a crescent-shaped curve as shown in Fig.7(a) and (c) for which proper voltages are ap-

plied.

If the drift time is affected by δ-rays, distortions in the t_1-t_2 plot will appear. Specifically, if δ-rays travel closer to the fired sense wire than the heavy ions, the δ-rays will cause earlier signals and shorten the drift time. This feature can be seen in the lower part of the curve in Fig.7(b) when a higher voltage is applied. On the other hand, δ-rays may also activate sense wires not traversed by the heavy ions and produce false signals with larger drift time clearly visible in the upper right of the curves in Fig.7(b).

Given the relatively low charge of δ-rays, the number of primary ionized electrons they produce in the drift chamber is limited. At lower voltages, the primary electrons are more prone to recombination with the gas, which hinders the generation of signals from δ-rays on the sense wire. In contrast, at higher voltages, δ-rays more readily produce signals, resulting in a greater impact. Consequently, the distortion of the t_1-t_2 distribution observed in Fig.7(b) is greater than that in Fig.7(a). Since particles with larger Z are easier to emit δ-rays as they pass through the drift chamber, the distortion is more pronounced for $Z = 36$ compared to $Z = 20$ at the same voltage.

VI. MULTIPLICITY

The distributions of the multiplicity (M) for the fired sense wires in a layer are investigated. Fig.8 shows the proportion of M as functions of Z and U for the FDC. Here, $M = 0$ indicates that the wire layer was unable to detect the particle as it entered the chamber. In contrast, $M > 1$ suggests that a single incident particle has generated multiple signals in the wire layer, mainly caused by erroneous signals from δ-rays. The impact of δ-rays on the drift chamber is weak when $P(M = 1)$, defined as the proportion of events with $M = 1$, is high.

Fig.8(a) illustrates $P(M = 1)$ and $P(M > 1)$ as functions of Z value for the FDC at $U = 900$ V. It can be seen that $P(M = 1)$ decreases as Z increases. This is because an increase of Z results in an increase of emission of δ-rays by the beams in the gas [25, 26]. This increase in δ-rays leads to a rise of in $P(M > 1)$ and a reduction in $P(M = 1)$.

Fig.8(b) shows $P(M = 1)$ and $P(M > 1)$ as functions of voltage for the FDC at $Z = 36$. When the voltage is low, a moderate increase in voltage enhances the drift chamber's detection efficiency. While the voltage exceeds a certain threshold (750 V, as shown in Fig.8(b), the influence of δ-rays becomes more pronounced, causing a significant decrease in $P(M = 1)$.

VII. THE r-t RELATION

The drift distance-drift time (r-t) relation enables the calculation of the distance from the initial ionization position to the sense wire, thus allowing the position of the particle to be determined. Due to the significant dependence of electron drift velocity in the drift chamber on factors such as the working gas and voltage, the r-t relation varies under different conditions. Consequently, distinct r-t relations need to be employed for various scenarios.

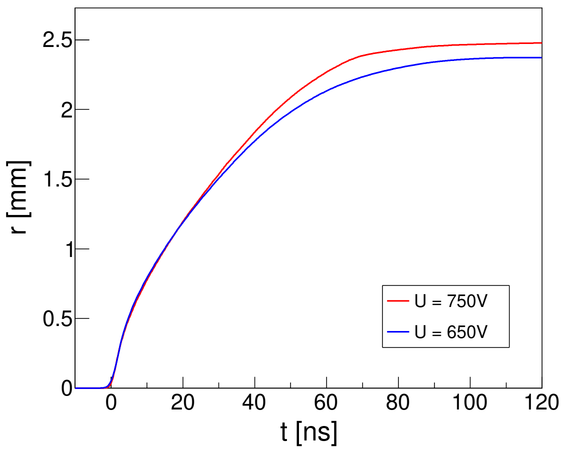

Fig. 9. The r-t relations of FDC for $Z = 36$ at $U = 750$ V (red line) and $U = 650$ V (blue line).

For the parameterization of the r-t relation, a commonly used method involves simulating an initial r-t relation and iteratively obtaining the final r-t relation through polynomial fitting [27, 28]. However, the function obtained through the iterative method struggles to capture the irregularities caused by the non-uniform electric field at the edges of the drift chamber. Another method to obtain the r-t relation is through the integrated drift time spectrum [25]. Under the condition of uniformly incident particles, this method better reflects the irregularities of the electric field within the drift chamber.

In the present experiment, the beam spot can cover multiple drift cells. For the entire drift chamber, the distance r from the particles to the sense wire can be approximately considered as uniformly distributed. Therefore, we adopt the method of integrating the drift time spectrum to obtain the r-t relations.

Assuming that the probability density function of the drift time spectrum is represented by $f(t)$, and the probability density function of drift distance is $g(r)$. The relationship between $g(r)$ and $f(r)$ can be expressed as

$$g(r)dr = f(t)dt, \tag{1}$$

and the drift velocity $v(t)$ can be obtained from the formula

$$v(t) = dr/dt = f(t)/g(r). \tag{2}$$

If the drift distance is uniformly distributed, then $g(r) = 1/d$, where d represents the maximum drift distance of primary electrons. Thus, $v(t)$ can be expressed as $v(t) = f(t)d$. Consequently, the r-t relation function $r(t)$ can be obtained as

$$r(t) = \int_0^t v(\tau)d\tau = d\int_0^t f(\tau)d\tau. \tag{3}$$

The upper limit of the r-t relation is d, and its value is related to the proportion of $M \geq 1$ ($P(M \geq 1)$). Events

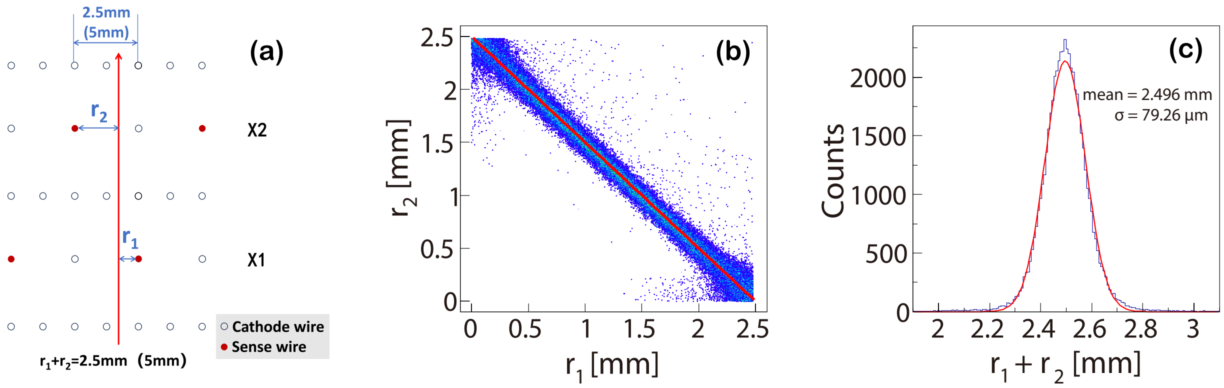

Fig. 10. (a) Relation of r_1 and r_2 for tracks perpendicular to X1 and X2 of FDC (RDC). $r_{1(2)}$ represents distance from the particle track to the sense wire of the drift cell crossed by the track in X1(2); (b) scatter plot of r_1 and r_2 in FDC derived from r-t relation at $U = 750$ V and $Z = 36$, with the red line $r_1 + r_2 = 2.5$ mm superimposed; (c) distribution of $r_1 + r_2$, fitted with a Gaussian (red line).

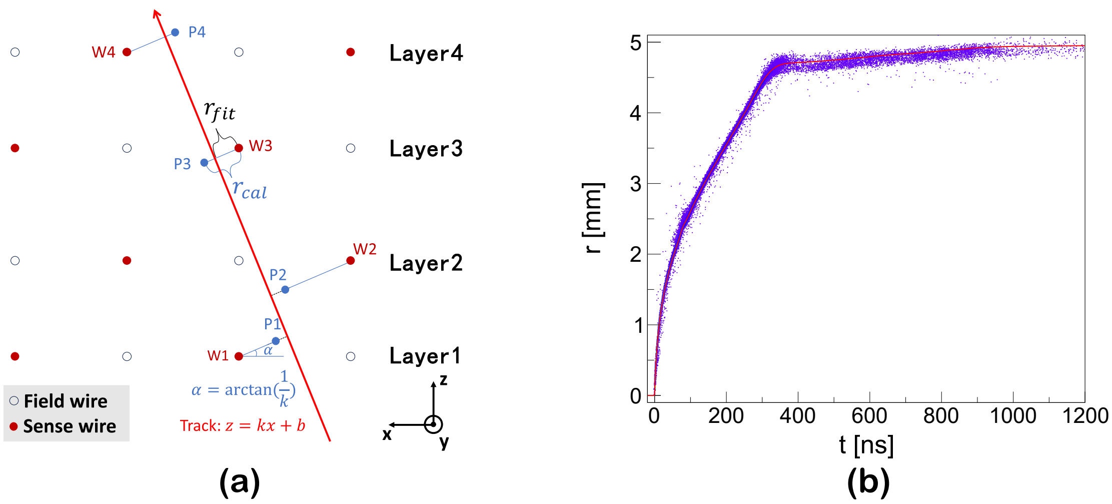

Fig. 11. (a) Illustration of the tracking fitting; (b) r-t relation of RDC at $U = 700$ V and $Z = 36$. Scattered points are predicted from track fitting and the red line is obtained from integrating the drift time spectrum.

where the distance between the primary electrons and the sense wires exceeds d cannot generate signals ($M = 0$), resulting in a loss of $P(M \geq 1)$. Therefore, d can be expressed as

$$d = L \cdot P(M \geq 1), \qquad (4)$$

where L represents the length of the drift unit. For FDC (RDC), $L = 2.5$ mm (5 mm). The detection efficiency varies under different conditions (see Fig.8), and d also changes accordingly.

Fig.9 shows the r-t relation of FDC derived from the integral drift time spectrum method under two different applied voltages $U = 750$ V and $U = 650$ V. The $P(M \geq 1)$ at 750 V and 650 V are 98.9% and 92.8% (see Fig.8(b), with the corresponding upper limits $d = 2.47$ mm and 2.32 mm, respectively.

The quality of the obtained r-t relation can be evaluated based on the correlation of two drift distances r_1-r_2 deduced from adjacent two layers. For particles incident perpendicular to the sense wire plane, the $r_1 + r_2 = 2.5$ mm (5 mm) relation for the FDC(RDC) should be fulfilled, as illustrated in Fig.10(a).

The scatter plot of r_1 and r_2 for the FDC obtained from the beam test is presented in Fig.10(b). It can be seen that the r_1-r_2 relation shows a linear trend consistent with the $r_1 + r_2 = 2.5$ mm relation (red line), indicating the rationality of the r-t relation. Due to the divergence of beam's angle and drift time uncertainty, there is a small broadening in the r_1-r_2 distribution. Fig.10(c) shows the projection of Fig.10(b) onto the line $y = x$, exhibiting a Gaussian distribution with a mean of 2.496 mm.

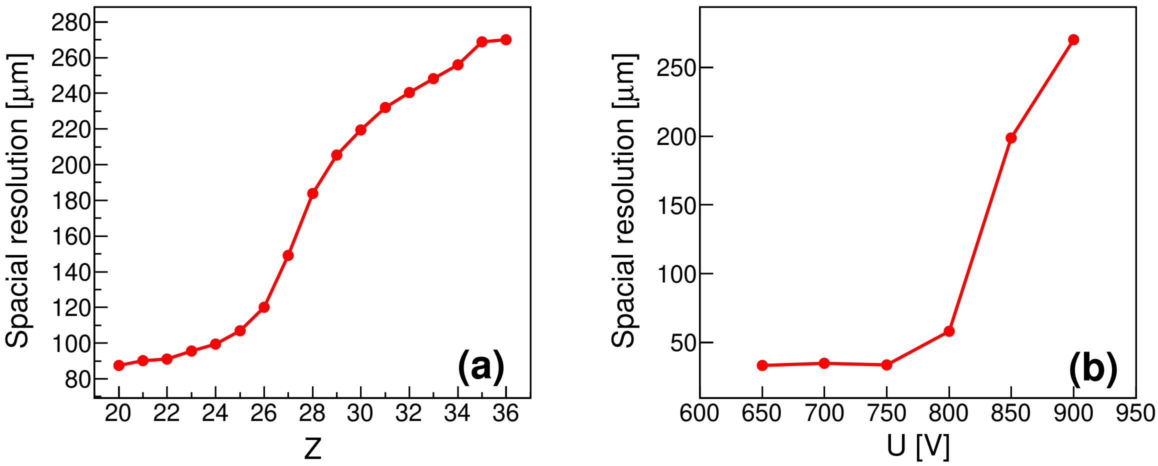

Fig. 12. The spatial resolution of RDC as functions of Z at $U = 900$ V (a) and U at $Z = 36$ (b).

VIII. BEAM TRACKING AND SPATIAL RESOLUTION

In nuclear physics experiments, reconstruction of the ion's trajectory plays an important role in the high-precision position and momentum measurements [29, 30], as well as the identification of charged particles. In the ETF target area, particle tracks are divided into two sections: before and after the target. The FDCs and RDCs are employed to reconstruct the tracks for each section.

The track fitting is performed using signals from the four layers of wires in the two FDCs (RDCs), with at least three layers of signals required. First, the fired points are assumed to be at the positions of the fired sense wires labeled as W1—W4 for the four layers in Fig.11(a). The initial track is obtained by fitting the assumed fired points using the least squares method. The position of an updated fired points P1—P4 can be calculated by using the initial track information and the drift distance r^i_{cal} derived from the r-t relation of the i-th layer, as depicted in Fig.11(a). An updated track then can be obtained by fitting the updated fired points. The points P1—P4 and the track will be iteratively updated.

The distance from the track to the fired sense wire of the i-th layer is denoted as r^i_{fit}. And the residual is defined as the difference between r^i_{fit} and r^i_{cal}, it can be expressed as

$$\chi_i = r^i_{fit} - r^i_{cal}. \tag{5}$$

Then the sum of squared residuals is expressed as

$$\chi^2 = \sum_i (r^i_{fit} - r^i_{cal})^2. \tag{6}$$

The track iteration process is repeated multiple times until the sum of the squared residuals reaches its minimum. This fitting process essentially works like finding the common tangent to the circles centered at W1—W4 with r^i_{cal} as their radii [31].

The scattered points in Fig.11(b) represent r_{fit}-t in RDC, with the employed r_{cal}-t relation superimposed. The degree of conformity between the scattered points and r_{cal}-t relation reflects the quality of the fitted tracks. The majority of the scattered points generated by the fitted tracks form a band that aligns well with the r_{cal}-t relation. It can be observed that at drift distances greater than 4.5 mm, the electron drift time becomes significantly prolonged due to the weak electric field and the meandering of the field lines [32].

The spatial resolution of the drift chamber can be characterized by the standard deviation (σ) of the residual distribution [33–35]. Fig.12(a) shows the measured spatial resolution as a function of beam's charge Z at $U = 900$ V. It is evident that the resolution becomes worse as Z increases, which is due to particles with higher Z emitting more δ-rays under the same voltage condition.

At a low voltage, particles with higher Z achieve better spatial resolution [36]. However, when the voltage is excessive, the influence of δ-rays increases, resulting in a rapid deterioration of spatial resolution. This feature can be clearly seen in Fig.12(b) for particle of $Z = 36$. Therefore, for particles with a high Z, the voltage can be moderately reduced in order to reduce the impact of δ-rays and improve the spatial resolution. At a voltage of approximately 700 V, the drift chamber achieves its optimal spatial resolution of 35 μm.

IX. SUMMARY

We have constructed the FDCs and RDCs for tracking of incoming and outgoing beam at the target area of ETF. The spatial resolution of FDCs (RDCs) is crucial for precise track reconstruction and particle identification. This article provides an overview of the construction details of FDCs (RDCs). Through beam tests, the effects of the time walk and δ-rays on the drift time were investigated. The performance of the drift chamber was evaluated under different voltages,

with a particular focus on the impact of δ-rays on resolution. The test results indicate that the effects δ-rays are more pronounced at high voltages and with ions that have large Z values, leading to a decrease in the spatial resolution and the number of events with a multiplicity of 1 of the drift chamber. On the other hand, an insufficient voltage can lead to a decrease in the number of events with multiplicity greater than 0, resulting in fewer particles detected by the drift chamber. Therefore, an appropriate voltage must be chosen based on the nuclear charge number of the particles under investigation. At the optimal voltage, the FDCs (RDCs) achieves a resolution of approximately 35 μm.

[1] W. Blum, L. Rolandi, Particle Detection with Drift Chambers (Springer, Berlin, 1994), p.120.

[2] Z.B. He, Z. Qin, P. Ma et al., Development of a MWDC prototype of the CSR external-target experiment. Nucl. Sci. Tech. **35**, 174, (2024). doi:10.1007/s41365-024-01515-0

[3] L. He, S.Y. Luo, X.M. Liu et al., Simulation and experimental comparison of the performance of four-corner-readout plastic scintillator muon-detector system. Nucl. Sci. Tech. **35**, 188, (2024). doi:10.1007/s41365-024-01530-1

[4] T. Kobayashi, N. Chiga, T. Isobe et al., Samurai spectrometer for ri beam experiments. Nucl. Instr. and Meth. B **317**, 294–304 (2013). doi: 10.1016/j.nimb.2013.05.089

[5] D. Bazin, J.A. Caggiano, B.M. Sherrill et al., The s800 spectrograph. Nucl. Instr. and Meth. B **204**, 629–633, (2003). doi: 10.1016/S0168-583X(02)02142-0

[6] W.L. Zhan, H.S. Xu, G.Q. Xiao et al., Progress in HIRFL-CSR. Nucl.Phys. A **834**, 694c–700c, (2010). doi:10.1016/j.nuclphysa.2010.01.126

[7] S.W. Tang, S.T. Wang, L.M. Duan et al., A tracking system for the external target facility of CSR. Nucl. Sci. Tech. **28(5)**, 68, (2017). doi:10.1007/s41365-017-0217-8

[8] X.W. ZHAO, Y. QIAN, J. KONG et al., Readout electronics for CSR-ETF silicon strip array detector system. Nuclear Science and Techniques. Nucl. Sci. Tech. **25(4)**, 040402, (2014). doi:10.13538/j.1001-8042/nst.25.040402

[9] Y. Yuan, J. Yang, J. Xia et al., Status of the HIRFL-CSR complex. Nucl. Inst. Meth. B **317**, 21, (2013). doi:10.1016/j.nimb.2013.07.040

[10] J.W. Xia, W.L. Zhan, B.W. Wei et al., The heavy ion cooler-storage-ring project (HIRFL-CSR) at Lanzhou. Nucl. Instr. and Meth. A **488**, 11–25, (2002). doi:10.1016/S0168-9002(02)00475-8

[11] Z. Xiao, L.W. Chen, F. Fu et al., Nuclear matter at a HIRFL CSR energy regime. J. Phys. G Nucl. Partic. **36**, 064040 (2009). doi:10.1088/0954-3899/36/6/064040

[12] B.H. Sun, J.W. Zhao, X.H. Zhang et al., Towards the full realization of the RIBLL2 beam line at the HIRFL-CSR complex. Sci. Bull. **63(2)**, 78–80, (2018). doi:10.1016/j.scib.2017.12.005

[13] F. Fang, S.W. Tang, S.T. Wang et al., Improving the Particle Identification of Radioactive Isotope Beams at the RIBLL2 Separator. Nucl. Phys. Rev. **39**, 65–72, (2022). doi:10.11804/NuclPhysRev.39.2021035

[14] C.L. Guo, G.L. Zhang, W.W. Qu et al., Simulation of (p,d) reaction on RIBLL2 for study of tensor force. Nucl. Sci. Tech. **26(4)**, 040501, (2015). doi:10.13538/j.1001-8042/nst.26.040501

[15] X.H. Zhang, S.W. Tang, P. Ma et al., A multiple sampling ionization chamber for the External Target Facility. Nucl. Instr. and Meth. A **795**, 389–394, (2015). doi:10.1016/j.nima.2015.06.022

[16] Y.Z. Sun, Z.Y. Sun, S.T. Wang et al., The charged fragment detector system of the External Target Facility. Nucl. Instr. and Meth. A **927**, 390–395, (2019). doi:10.1016/j.nima.2019.02.067

[17] A. Badala, M. La Cognata, R. Nania et al., Trends in particle and nuclei identification techniques in nuclear physics experiments. La Rivista Del Nuovo Cimento **45(3)**, 189276, (2022). doi:10.1007/s40766-021-00028-5

[18] J.H. Liu, Z. Ge, Q. Wang et al., Electrostatic-lenses position-sensitive TOF MCP detector for beam diagnostics and new scheme for mass measurements at HIAF. Nucl. Sci. Tech. **30**, 152, (2019). doi:10.1007/s41365-019-0676-1

[19] M.Y. Yang, Y. Qian, T.L. Pu et al., Edims: an event-driven internal memory synchronized readout prototype ASIC chip developed for HFRS-TPC. Nucl. Sci. Tech. **34**, 196, (2023). doi:10.1007/s41365-023-01341-w

[20] E. Delagnes, P. Abbon, Y. Bedfer et al., SFE16, a low noise front-end integrated circuit dedicated to the read-out of large Micromegas detectors. IEEE Trans. Nucl. Sci. **47(4)**, 1447–1453, (2000). doi:10.1109/23.872994

[21] J. Christiansen., HPTDC High Performance Time to Digital Converter. Technical report, (CERN, Geneva, 2004).

[22] L. Zhao, L.F. Kang, J.W. Zhou et al., A 16-Channel high-resolution time and charge measurement module for the external target experiment in the CSR of HIRFL. Nuclear Science and Techniques. Nucl. Sci. Tech. **25**, 010401, (2014). doi:10.13538/j.1001-8042/nst.25.010401

[23] M. Simon, M. Henkel, R. Hundt et al., A drift chamber telescope for heavy ion track detection. Nucl. Instr. and Meth. **221(2)**, 466–471, (1984). doi:10.1016/0167-5087(84)90021-8

[24] M. Hof, J. Isbert, K.D. Mathis et al., A drift chamber telescope for heavy ion track detection with high spatial resolution. Nucl. Instr. and Meth. A **276(3)**, 628–635, (1989). doi:10.1016/0168-9002(89)90596-2

[25] F. Sauli., Principles of operation of multiwire proportional and drift chambers. Technical report, (CERN, Geneva, 1977).

[26] T. Kobayashi, F.S. Bieser, T.J.M. Symons et al., A drift chamber for high-energy heavy ions. Nucl. Instr. and Meth. A **254(2)**, 281–302, (1987). doi:10.1016/0168-9002(87)90676-0

[27] H. Hirano, M. Akatsu, Y. Fujita et al., A high-resolution cylindrical drift chamber for the KEK B-factory. Nucl. Instr. and Meth. A **455(2)**, 294–304, (2000). doi:10.1016/S0168-9002(00)00513-1

[28] A. Ferrari., The KLOE drift chamber. Nucl. Instr. and Meth. A **494**, 163–172, (2002). doi:10.1016/S0168-9002(02)01461-4

[29] M.Y. Liu, W.D. Li, X.T. Huang et al., Simulation and reconstruction of particle trajectories in the CEPC drift chamber. Nucl. Sci. Tech. **35(8)**, 128, (2024). doi:10.1007/s41365-024-01497-z

[30] Q.G. Liu, S.L. Zang, W.G. Li et al., Track reconstruction using the TSF method for the BESIII main drift chamber. Chin. Phys. C **32(7)**, 565, (2008). doi:10.1088/1674-1137/32/7/011

[31] L.M. Lyu, H. Yi, L.M. Duan et al., Simulation and prototype testing of multi-wire drift chamber arrays for the CEE. Nucl. Sci. Tech. **31**, 11, (2020). doi:10.1007/s41365-019-0716-x

[32] X.L. Kang, L.H. Wu, Z. Wu et al., Calibration study of the X-T relation for the BESIII drift chamber. Chin. Phys. C **39(2)**, 026002, (2015). doi:10.1088/1674-1137/39/2/026002
[33] B. Hong, J.K. Ahn, G. Bak et al., Development of large acceptance multi-purpose spectrometer in Korea for symmetry energy. Nucl. Sci. Tech. **29**, 171, (2018). doi:10.1007/s41365-018-0507-9
[34] H.L. Wang, Z. Wang, C.S. Gao et al., Design and tests of the prototype beam monitor of the CSR external target experiment. Nucl. Sci. Tech. **33**, 36, (2022). doi:10.1007/s41365-022-01021-1
[35] M. Huang, J.Y. Zhu, and J. Wu, Study of spatial resolution of the associated alpha particle imagingtime-of-flight method. Nucl. Sci. Tech. **30**, 64, (2019). doi:10.1007/s41365-019-0580-8
[36] H. Miya, S. Ota, T. Fujii et al., Development of low-pressure multi-wire drift chambers for high-resolution spectroscopy with radioactive isotope beams. Nucl. Instr. and Meth. B **317**, 701–704, (2013). doi:10.1016/j.nimb.2013.08.018